Solid State Sciences, Volume 102, April 2020, Article number 106164
DOI:10.1016/j.solidstatesciences.2020.106164

Synthesis of Eu^{3+}-doped ZnO/Bi2O3 heterojunction photocatalyst on graphene oxide sheets for visible light-assisted degradation of 2,4-dimethyl phenol and bacteria killing

Pooja Shandilya[a,b], Anita Sudhaik[a], Pankaj Raizada[a,b], Ahmad Hosseini-Bandegharaei[c,d], Pardeep Singh[a], Abolfazl Rahmani-Sani[c,**] Vijay Thakur[e***]*

[a]*Schoolof Chemistry, Faculty of Basic Sciences, Shoolini University, Solan(HP)-173229, India*

[b]*Himalayan Centre for Excellence in Nanotechnology, Shoolini University. Solan (HP) India-173229*

[c]*Department of Environmental Health Engineering, Faculty of Health, Sabzevar University of Medical Sciences, Sabzevar, Iran*

[d]*Department of Engineering*, Kashmar Branch, Islamic Azad University, PO Box 161, Kashmar, Iran

[e]*Enhanced Composites and Structures Center, School of Aerospace, Transport and Manufacturing, Cranfield University, Bedfordshire MK43 0AL, UK*

*Email:*pardeepchem@gmail.com, **rahmani240@gmail.com),*
****vijay.kumar@cranfield.ac.uk*

Abstract

We reported the immobilization of binary heterojunction Eu^{3+}-ZnO/Bi_2O_3 over the surface of graphene oxide (GO) sheets by precipitation method to compose a visible light drive photocatalyst.

The ternary nanocomposites were characterized by different spectral technique like FESEM, FTIR, XRD, XPS, EDX, HRTEM, UV-visible, PL, HPLC and LCMS analysis. The high specific surface area of 106.0 m^2g^{-1} of Eu^{3+}-ZnO/Bi_2O_3/GO nanocomposites was ascertained by BET adsorption-desorption isotherm. The nano-composite exhibit excellent photo-efficiency for the photodegradation of 2, 4-dimethyl phenol (DMP) under visible region and was almost completely mineralized in 100 min as compared to the bare and binary system. The mineralized products of DMP were analyzed by HPLC and LCMS analysis. The kinetic model suggests the degradation pathway obeys pseudo-first order kinetic. Their antibacterial property were assessed against *E. coli* bacteria and nearly 90% of gram negative bacteria were killed by using ternary photocatalyst as determined by CFU method. Also, Eu^{3+}-ZnO/Bi_2O_3/GO nanocomposites possessed significant recycle efficiency up to six consecutive cycles which is beneficial to minimize the tariff. The improved photo-efficiency is due to the extension towards visible region, increase surface area, and high charge separation in ternary heterojunction.

Keywords: Eu^{3+}doped ZnO; Bi2O3; Heterojunction formation; Enhanced photo-catalysis; 2,4-dimethylphenol degradation; Antibacterial activity

Introduction

Phenols and their derivative is a primary pollutant released by the various industries like paint, textiles, paper, plastics, petroleum refining and pharmaceutical industries etc. [1]. The existence of phenolic compounds in waste water need to be eliminated as it brings a lots of harmful effects on human health and aquatic life. To address this, advanced oxidation processes (AOPs) have found a valuable potential for the degradation of various pollutant in aqueous suspension [2]. Amongst, AOP's process employed for the organic pollutants degradation, visible light assisted photocatalysis is of the most appropriate ones, owning to its several advantages like inexpensiveness and effectiveness. Among the various semiconductors used for photocatalytic processes, zinc oxide (ZnO) has emerged as a suitable catalyst for photocatalytic degradation and mineralization of various organic and inorganic contaminants [3]. The excellence of ZnO is due to its strong oxidizing power and low cost which makes it a favorable candidate to carry out photocatalytic oxidation processes occurring in water media [4]. On exposure to solar light with energy higher or equal to the band gap of ZnO semiconductor, generation of electron-hole pair takes place. The generated electrons reacts with O_2 to form superoxide radicals ($O_2^{\bullet -}$) and meanwhile, the holes reacts with H_2O or OH^- ions to produce hydroxyl radicals ($^{\bullet}OH$) [5, 6]. Owing to strong oxidizing ability, $^{\bullet}OH$ and $O_2^{\bullet -}$ degraded the pollutant and convert them into H_2O and CO_2 [7]. However, ZnO is only active under UV light, and it also suffers from re-combination of charge carrier produced during photocatalysis [8]. To overcome these drawbacks of ZnO and similar semiconductors, till now, two main strategy have been employed: (i) doping with cationic, anionic or rare earth elements and (ii) the construction of heterojunction with other semiconductors [9–11]. These strategy aims to enhance the stability, photocatalytic efficacy and expand the absorption of light in visible range. Nowadays, doping with a rare earth element, like Ln^{3+} ion, has

been revealed that can cause improvement in the ZnO photocatalytic activity [10]. Khataee *et al.* prepared Eu^{3+} doped ZnO nanoparticles by using the sonochemical method and was exploited for the photo-degradation of acid orange dye [10]. Similarly, Aneesh et al. prepared Eu^{3+} doped ZnO nanoparticles with various amounts of Eu-dopant, in which the luminescence quenching of ZnO nanoparticles was enhanced with increase in doping concentration of Eu [11].

On other hand, bismuth oxide (Bi_2O_3) is more advantageous and emerges as noble photocatalyst with a band gap of ~1.75–2.8 eV active under visible light region [12, 13]. It is an attractive compound with variety of application in electronics, fuel cells, ceramics, gas sensors and catalyst etc. Earlier, Bi_2O_3 has already been utilized to boost the photocatalytic activity of metal oxide semiconductor photocatalysts. For instance, Balachandran and Swaminathan prepared a series of α-Bi_2O_3/ZnO nanocomposites with variable amounts of α-Bi_2O_3 (6.8–18.9 wt %) and used them for photodegradation of acid red dye [14]. Similarly, Yang et al. reported the fabrication of ZnO nano-fibers and β-Bi_2O_3 heterostructure and utilized it for Rhodamine B dye photodegradation under both UV and visible light [15]. Due to low band gap and high rate of recombination of bare Bi_2O_3 photocatalyst, limits its application to use as efficient photocatalyst. Thus formation of heterojunction is an effective strategy for constructing visible light active photocatalyst and also to mitigate the rate of electron-hole pair recombination. Coupling two semiconductor with suitable energy gap and band edge potential to enhance the photoefficiency is the sole criteria for forming heterojunction Here, the valence band edge and conduction band edges of Bi_2O_3 make it suitable for the coupling with Eu^{+3}-ZnO.

Recently, carbon material is acquiring lots of attention due to their versatile properties. The various carbon derived material utilized so far as a supportive material for binary heterojunction were graphene, graphene oxide, carbon nanotube, fullerene, activated carbon etc. Large specific

surface area, high electrical and thermal conductivity, and facile charge carrier mobility make graphene oxide more advantageous to be utilized in combination with different binary and ternary heterojunction for enhanced photo-efficiency [16]. In the present work, the follow-up of our previous studies is continued in the field of graphene-based composites for photodegradation of organic contaminants in aqueous suspension. Eu^{3+} doped ZnO was coupled with Bi_2O_3 which in turn dispersed onto graphene oxide (GO) surface and the fabricated composite were then utilized for photodegradation of DMP in water samples. Eu^{3+}-ZnO/Bi_2O_3/GO photocatalyst was comprehensively characterized by FESEM, TEM, XRD, EDX, UV-visible techniques, along with photoluminescence (PL) analysis. Due to the toxicity, carcinogenic nature, and resistance towards degradation of DMP, it was photodegraded by utilizing Eu^{3+}-ZnO/Bi_2O_3/GO. Further, the degradation kinetics followed by most plausible mechanism for the increased photocatalytic efficiency of the ternary heterojunction was also proposed. Lastly, recycle efficiency of Eu^{3+}-ZnO/Bi_2O_3/GO up to six catalytic cycle was also assessed for DMP degradation.

2. Experimental

2.1. Fabrication of Eu^{3+}-ZnO/Bi_2O_3/GO

Here, advanced Hummer method were executed to synthesize graphene oxide as per previously reported work [16]. Eu^{3+} doped ZnO was prepared using the sonochemical method [17]. Typically, $ZnCl_2$ (1 g) and of $C_6H_9EuO_6 \cdot xH_2O$ (0.1 g) were dissolved in 100 mL of distilled water. To this reaction mixture, NaOH (1M) was added to maintain pH 10 and the mixture was subjected to ultrasonication for 1 h. The obtained white precipitates were rinsed with ethanol and deionized water and dried at 80 ˚C in hot air oven. ZnO was prepared by the same procedure without addition of $C_6H_9EuO_6 \cdot xH_2O$. In order to prepare Eu^{3+}-ZnO/Bi_2O_3/GO, GO (1 g) was dispersed in distilled water (100 mL) with sonication for half an hour. To this suspension, 1.0 g $Bi(NO_3)_3$ and 30 mL

NH_4OH (1 M) were added with continuous stirring. In the next step, 0.5 g Eu^{3+}-ZnO was added to the reaction solution followed by sonication for 1 h. Eventually, precipitates were separated and washed with water, dried at 80 ˚C to obtain Eu^{3+}-ZnO/Bi_2O_3/GO composite. The same route was exploited to prepare Bi_2O_3 with no addition of GO and Eu^{3+}-ZnO during the course of the reaction. GO was used as support for Eu^{3+}-ZnO/Bi_2O_3 nanoparticles with even dispersal of Eu^{3+}-ZnO/Bi_2O_3 and low agglomeration over its surface.

2.2. Apparatus

Transmission electron microscopy (TEM) pictures was captured on a randomly selected area at voltage of 200 kV, using FP/5022-Tecnai G2 20 S-TWIN (USA) instrument. A Nava Nano SEM-45 (USA) instrument was applied for recording the scanning electron microscopy (SEM) micrographs. A Perkin-Elmer Spectrometer (Spectrum RX-l) with KBr pellet was used for recording the FTIR spectra ranges from 4000-400 cm^{-1}. A Panalytical's X'Pert Prodiffractrometer with CuK-α-1 (45 kV/100 mA) source was used for recording X-ray diffraction (XRD) patterns. To estimate the optical absorption performance, using $BaSO_4$ as the reference, a diffuse reflectance spectrophotometer (UV 3600, Shimadzu) was employed. A Coulter SA3100 instrument was exploited for determination of the BET surface area of the sample by the aid of Nitrogen adsorption-desorption isotherms. A FLS-920 instrument (Edinburgh) was employed for recording the photoluminescence (PL) spectra. A digital lux-meter (750 lx) was used for the measurement of light intensity. For the analysis of degradation product during mineralization, a test were performed on a Water HPLC instrument (Austria) utilizing a C_{18} column (5µm, 25cm length and 7mm diameter) and taking a 1:39:60 ratio of acetic acid: methanol: water as eluent with a flow rate of 0.5 mL min^{-1}. The LCMS information was obtained for analyzing degradation products using JEOL GCMATE II GC-MS with a high-resolution data system**.**

2.3. Photocatalytic activity of Eu^{3+}-ZnO/Bi_2O_3/GO for DMP degradation

The photocatalytic experiment were conducted in a self-developed photoreactor. Details of photoreactor are given in our previous work [18]. The estimation of chemical oxygen demand analysis was done using the reflux technique [19]. CO_2 was estimated by titration of the reaction mixture with NaOH solution [20]. The DMP removal percentage was computed using Eq. (1).

$$\%\ \text{removal effciency} = \frac{C_0 - C_t}{C_0} \times 100 \quad (1)$$

Where, C_t and C_0 are the instant and initial concentrations/COD of DMP, respectively.

3. Results and discussion

3.1. Morphology and structure characterization of Eu^{3+}-ZnO/Bi_2O_3/GO

The FESEM images of GO and Eu^{3+}-ZnO/Bi_2O_3/GO are laid out in Fig. 1 a-d. The graphene oxide exfoliation can be observed in Fig.1 a. Fig. 1b shows the thin, wrinkled, non-uniform and highly porous GO surface. The porous surface of GO facilitates the adsorption of organic pollutants present in the aqueous phase. In Fig. 1c, dispersion of Eu^{3+}-ZnO/Bi_2O_3 photocatalyst onto GO surface can be clearly dipicted. As can be seen in high magnification FESEM image, the agglomerates of Eu^{3+}-ZnO/Bi_2O_3 are of different size and shape (Fig.1d). HRTEM analysis further ascertained the deposition of Eu^{3+}-ZnO and Bi_2O_3 on porous GO sheets (Fig.2a and b). The lattice fringes at 0.33 nm, 0.28 and 0.26 nm was ascribed to (120), (001) and (002) plane of Bi_2O_3, ZnO and GO respectively [21-22]. Selected area electron diffraction (SAED) analysis confirmed the polycrystalline nature of the prepared photocatalyst (Fig. 2c). Fig. 2d explains the interplanar spacing between the two layers of Eu^{+3}-ZnO/Bi_2O_3/GO is 0.28 nm which

indicate the successful incorporation of Eu^{+3}-ZnO/Bi_2O_3 over graphene oxide sheet comparable with previously reported works [22].

The XRD spectrum of Eu^{3+}-ZnO/Bi_2O_3/GO is exhibite in Fig. 3a. The diffraction peaks labeled with ♥ at 2θ = 26.6°, 49.9°, and 48° were assigned to {120}, {200} and {433} planes of Bi_2O_3, respectively [13]. The diffraction peak of GO, denoted with ♦ at 2θ = 26.2°, was due to {002) plane of GO [2]. The XRD peaks leveled with ● at 31°, 34°, 37°, 47.6°, 56°, 63°, 65 °, and 70° were assigned to {100}, {002}, {101}, {102}, {110},{103}, {102) and {112} planes present in Eu^{3+}-ZnO [10]. FTIR spectrum of Eu^{3+}-ZnO/Bi_2O_3/GO is shown in Fig. 3b. The band at 525 was due to Zn-O stretching vibration [23]. The peaks at 1405, 1650 and 1020 cm^{-1} were due to C-H (bending vibration), C=O and C-O-C stretching vibrations, respectively [24]. The peak at 862 cm^{-1} was due to Bi-O stretching vibration present in Bi_2O_3 [13]. The peak at 3435 was assigned to O-H stretching of adsorbed water molecules [25]. The atomic percentage of Zn, Bi, Eu, C and O is 6.7, 4.5, 0.54, and 55.70, 32.97 as depicted by EDX analysis (Fig. S1). The analysis of these results confirmed the formation of Eu^{3+}-ZnO/Bi_2O_3/GO.

To confirm the structural changes in GO after oxidation a Raman spectra of GO were recorded between 500 and 2500 cm^{-1} as given in supplementary Fig. S2. The intensity of D and G band in the spectra clearly explain the formation of GO from graphite using Hummer's method. The D band determines the extent of disorder due to sp^3 hybridized carbon atom and G band determines the graphitic mode due to sp^2 carbon atom. The Raman spectra of graphite has two peak at 1366 cm^{-1} and 1598 cm^{-1} with I_D/I_G ratio 0.7. Whereas, the D and G band for GO is observed at 1364 cm^{-1} and 1607 cm^{-1} with I_D/I_G ratio 1.03. Broad D band is due to the addition of defects after oxidation. Further, the increase in I_D/I_G ratio from graphite to graphene oxide confirms the

incorporation of oxygen containing functional group. The observed peak is in good agreement the existing literature [26].

The XPS analysis further support the FTIR spectra. Fig. 4 displayed XPS spectra of Eu^{3+}-ZnO/Bi_2O_3/GO nanocomposites. Different elements present in nanocomposites were analyzed through XPS and provides information about chemical composition and oxidation states of different elements. Through XPS analysis, presence of Europium (Eu), Zinc (Zn), Bismuth (Bi), Oxygen (O) and Carbon (C) were confirmed in Eu^{3+}-ZnO/Bi_2O_3/GO nanocomposites. The high resolution spectra of C1s, O1s, Zn2p, Bi4f, and Eu3d core level could be observed in Fig. 4 (a-e). The binding energies at 1165 eV and 1135 eV were accredited to Eu $3d_{3/2}$ and Eu $3d_{5/2}$ orbital (Fig. 4a) [27]. These energy peaks confirms the presence of Eu (III) in synthesized nanocomposites. Zinc exhibited two sharp peaks at 1024 eV and 1043 eV binding energies which were assignable to Zn-$2p_{3/2}$ and Zn-$2p_{1/2}$ in Zn^{2+} state of ZnO and shown in Fig. 4b [28]. XPS spectrum of Bi 4f (Bi $4f_{5/2}$ and Bi $4f_{7/2}$) displayed in Fig. 4c possessed peaks at 158.6 and 164.5 eV [29]. Strong peak established at 530.5 eV was associated to O 1s orbital of oxygen atom (Fig. 4d) [30]. XPS spectrum of C1s showed sharp peaks at 283 and 288 eV were ascribed to sp^2 C-C bond and C-O bonds, respectively (Fig. 4e) [31]. The spectra confirmed the successful formation of Eu^{3+}-ZnO/Bi_2O_3/GO nanocomposites.

The UV-visible spectroscopy was utilized to assess the UV-visible light activity of Eu^{3+}-ZnO/Bi_2O_3/GO (Fig. 5a). ZnO had an absorption maximum at 368 nm with dominated absorption in the UV region [11, 15], which shows ultraviolet photo-response of ZnO. However, the absorption maximum showed a red shift and was observed at 410 nm in Eu^{3+} doped ZnO. Bi_2O_3 had an absorption edge at 438 nm [11, 14, 15]. In case of Eu^{3+}-ZnO/Bi_2O_3/GO, the absorption

198 edge was shifted to the visible region involving a red shift in absorption maximum. Tauc's plots
199 were plotted to find the band-gap energy of prepared photocatalyst using equation 2 [32].

200 $$\alpha h\upsilon = A(h\upsilon - E_g)^{n/2} \quad (2)$$

201 Where, index (n) can have 1, 2, 3, and 4 value for allowed direct and indirect electronic
202 transitions, and forbidden direct and indirect ones, respectively. Also, hν is photon energy in Tauc
203 equation and α symbol shows absorption coefficient. The band gaps of ZnO, Eu^{3+}-ZnO/Bi_2O_3/GO
204 and Bi_2O_3 are 3.36, 3.01, and 1.8 eV, respectively (Fig. 5b). The charge separation mechanism in
205 photocatalytic reaction was predicted by the photoluminescence analysis. ZnO had an emission
206 peak at 375 nm (Fig. 5c). The emission peaks intensity lowered in both Eu^{3+}-ZnO/Bi_2O_3 and Eu^{3+}-
207 ZnO/Bi_2O_3/GO. The decreased intensity of PL emission peak in Eu^{3+}-ZnO/Bi_2O_3/GO displayed
208 deferred rate of recombination as compared to Eu^{3+}-ZnO/Bi_2O_3 and ZnO, respectively. This
209 attribte to the electron engulfing nature of graphene oxide sheets towards charge carriers [2]. Fig.
210 5d shows nitrogen adsorption-desorption isotherms of Eu^{3+}-ZnO/Bi_2O_3/GO. The composite obeys
211 type IV isotherm with specific area of 106.0 m^2/g. This high specific surface area is highly suitable
212 for adsorption assisted photocatalytic degradation of the pollutant.

213 ***3.2. Photocatalytic activity of Eu^{3+}-ZnO/Bi_2O_3/GO for DMP degradation***

214 The photocatalytic activity of the composite was explored for the removal of DMP by the
215 aid of LED radiation. Fig. 6a exhibits photodegradation of DMP against the irradiation time period.
216 The simple light irradiation had no influence on the removal of DMP. The removal efficiencies of
217 99 %, 72 %, 51 %, 50 %, and 34 % were observed for Eu^{3+}-ZnO/Bi_2O_3/GO, Eu^{3+}-ZnO/Bi_2O_3, Eu^{3+}-
218 ZnO, ZnO and GO. Thus, the efficiencies of the exanimate materials followed the order Eu^{3+}-
219 ZnO/Bi_2O_3/GO> Eu^{3+}-ZnO/Bi_2O_3> Eu^{3+}-ZnO> Bi_2O_3> GO. The DMP removal experiments were
220 also conducted under the dark condition to evaluate the percentages removed by adsorption

process. Throughout the adsorption process alone, Eu^{3+}-ZnO/Bi_2O_3/GO, Eu^{3+}-ZnO/Bi_2O_3, Eu^{3+}-ZnO, ZnO, and GO had the respective efficiencies of 34, 8, 6, 9, and 32 % for DMP removal (Fig. 6b). The efficiency of the adsorbents followed the trend Eu^{3+}-ZnO/Bi_2O_3/GO> GO >Eu^{3+}-ZnO/Bi_2O_3>Eu^{3+}-ZnO> Bi_2O_3. The obtained result showed that Eu^{3+}-ZnO/Bi_2O_3/GO had the highest photocatalysis activity as well as the adsorption capability. The GO coupling with Eu^{3+}-ZnO/Bi_2O_3 increased the photo-catalytic degradation of DMP. This was because of notable adsorption of DMP onto graphene oxide sheets [16]. The kinetics of degradation were studied by Eq. (3) [33].

$$-\frac{dC}{dt} = kt \qquad (3)$$

Where, k is the rate constant, and C is DMP concentration at time t. This relation can be integrated between the limits of (0, C_0) and (t, C), from which one can have Eq. (4):

$$-\ln\left(\frac{C}{C_0}\right) = kt \qquad (4)$$

The graph between $-\ln(C/C_0)$ against time was used to find the value of rate constant. Eu^{3+}-ZnO/Bi_2O_3/GO, Eu^{3+}-ZnO, Bi_2O_3, and GO had the rate constant of 0.087, 0.050, 0.041, and 0.019, respectively. The R^2 values obtained were in the range 0.95-0.99 which indicated that pseudo-first order kinetic model was obeyed during the degradation processes. Both photocatalytic and adsorption experiments indicated that photocatalysis of DMP was significantly affected by adsorption process. So, further experiments were undertaken to find out the effect of adsorption on DMP degradation.

3.3. Effect of adsorption on the photo-catalytic activity of Eu^{3+}-ZnO/Bi_2O_3/GO

Fig. 7 shows the effectivness of the photocatalytic degrdation of DMP, using the composites, and compare their efficacy with adsoprtion ability alone, which is responsible for removal process. Fig.7 displays DMP removal under three reaction parameter. The first half of the graph display, adsorption of DMP without exposing towards light. The second half of the graph indicate simultaneous adsorption and photocatalysis (i.e. A+P process) where, 98 %, 72 %, and 32% of DMP was removed using Eu^{3+}-ZnO/Bi_2O_3/GO, Eu^{3+}-ZnO/Bi_2O_3, and GO, respectively. However, conducting photocatalytic process after adsorption (i.e. A-P process) the removal percentage of DMP in 3 h is 50 %, 68 %, and 34 % for Eu^{3+}-ZnO/Bi_2O_3/GO, Eu^{3+}-ZnO/Bi_2O_3, and GO, respectively. The order for various catalytic processes was revealed as: A+P > A-P > DA. During the A-P process, excessive adsorption of DMP on the surface of photocatalyst blocks penetration of light and decreases the total photoactive volume of the photocatalytic systems. The decreased photoactive volume causes a defamation of catalytic activity. By using the newly prepared composite, the concurrent adsorption and photocatalysis processes are the most efficient strategy for degrading DMP under visible light.

3.4. Mineralization study and recycling performance of Eu^{3+}-ZnO/Bi_2O_3/GO

The complete mineralization of DMP was assessed by determining COD estimation and CO_2 formation during photodegradation (Fig. 8a and b). COD was assessed using Eu^{3+}-ZnO/Bi_2O_3/GO assisted A+P process, while 65% and 64% removal were observed in the case of Eu^{3+}-ZnO and ZnO, respectively. Also, 78, 55, 20, and 2 mg/L of CO_2 were estimated during mineralization of DMP using Eu^{3+}-ZnO/Bi_2O_3/GO, Eu^{3+}-ZnO, Bi_2O_3, and GO photocatalyst, respectively. Both COD and CO_2 estimations are in agreement with each other. This confirms the complete mineralization of DMP into CO_2 and H_2O.

To explore the intermediate formed during the degradation of DMP, the HPLC analysis were estimated at different time intervals of 0h, 2h, 4h, 6h, 8h,10, respectively. After exposure to visible light, the decrease in intensity of peak at retention time nearly at 12 min was noticed for DMP as displayed in Fig 8c. Further, a group of new peaks (circled in Fig. 8c) appeared in between 2 to 4 minutes which subsequently vanished after certain time interval. The appearance of these peaks can be ascribed to the intermediates, developed during the mineralization process. In LCMS, peaks at 122, 150, 182, 108, 94, 88 116, and 46 shown in Fig. 9d were ascribed to 2,4-DMP, 2-hydroxy-5-formylbenzaldehyde, 4-hydroxyisophthalic acid, benzoquinone, phenol, oxalic acid, Maleic acid, and formic acid, respectively.

3.5. Band diagram and possible degradation mechanism

In order to understand the basic mechanism of enhanced photocatalysis in Eu^{3+}-ZnO/Bi_2O_3/GO, band positions of conduction band (CB) and valance band (VB) were determined exploiting Eq. (5) and (6) [34, 35]:

$$E_{VB} = \chi - E^e + 0.5\, E_g \quad (5)$$

$$E_{CB} = E_{VB} - E_g \quad (6)$$

Where, E_g represents the band gap of photocatalyst, E^e is equal to a constant value of 4.5 eV i.e. energy of free electron, and χ is electronegativity of semiconductor. The E_g and χ for Eu^{3+}-ZnO were 3.15 and 5.79 eV while for Bi_2O_3 it was found to be 1.8 and 5.59 eV, respectively [36-38]. The locations of VB and CB in Eu^{3+}-ZnO were 2.8 and -0.35 eV, respectively [36]. The position of VB and CB in Bi_2O_3 was found to be 1.30 and -0.54 eV, respectively [38].The band position of Eu^{3+}-ZnO and Bi_2O_3 was suited for formation of type II heterojunction with staggered band position. The scavenging examinations were conducted by utilizing isopropyl alcohol (IPA),

benzoquinone (BZQ), ammonium oxalate (AO), and Cr(VI) ion as hydroxyl radicals ($OH^{\bullet}$), superoxide radicals ($O_2^{\bullet-}$), holes (h^+_{VB}) and electrons (e^-_{CB}) scavengers, respectively [39].The removal efficiencies of 20, 54, 92, and 95 % were recorded in IPA, BZQ, Cr(VI), and AO, respectively as shown in (Fig. S3). The presence of Cr(VI) and AO had no remarkable influence on photocatalytic activity of Eu^{3+}-ZnO/Bi_2O_3/GO. During the scavenging experiment, whereas, $OH^{\bullet}$ and $O_2^{\bullet-}$ radicals showed the highest oxidizing strength for the degradation of DMP. The mechanism through which the new photocatalyst can mineralize DMP can be explained as follows (Fig. 9). Under visible light, holes, and electrons were produced in valance and conduction band of ZnO and Bi_2O_3 semiconductor, respectively. The migration of charge carrier takes place from the VB of Eu^{3+}-ZnO to VB of Bi_2O_3 in accordance with the position of its band potential. The band position of Eu^{3+}-ZnO and Bi_2O_3 was suited for formation of type II heterojunction with staggered band position. At the same time, photo-excited electrons migrate from CB of Bi_2O_3 to CB of Eu^{3+}-ZnO [40]. Due to this transfer, the recombining rate of photo-generated electron-hole pairs was diminished to a greater extent. The reaction of CB electrons of ZnO with adsorbed molecular O_2 led to production of superoxide ($O_2^{\bullet-}$) radicals on the surface. The hole in VB of Bi_2O_3 reacts with the H_2O molecule to produce hydroxyl radicals. The hydroxyl radicals and superoxide ultimately oxidized DMP into CO_2 and H_2O. Based on the obtained results, Eu^{3+}-ZnO/Bi_2O_3/GO emerged as a potential photo-catalyst for degradation of DMP present in water.

Recycling efficiency of the photocatalyst is very crucial for its long-term application in water purification process. The photo-catalyst was separated after each cycle thorough centrifugation process and utilized for the next photocatalytic cycle. After six catalytic cycles, the photo-efficiency of Eu^{3+}-ZnO/Bi_2O_3/GO was reduced from 98 to 89% (Fig. S4a). Furthermore, XRD, EDX and FITR analysis of Eu^{3+}-ZnO/Bi_2O_3/GO was performed (Fig. S4(b-d)). XRD, EDX

and FTIR spectra of Eu^{3+}-ZnO/Bi_2O_3/GO did not show any significant change in the crystalline structure of the ternary heterojunction even after six catalytic cycles. It indicates the long-term stability of prepared photocatalyst for DMP degradation.

3.6. Photocatalytic antibacterial activity of Eu^{+3}-ZnO/Bi_2O_3/GO

The photocatalytic antibacterial activity of Eu^{+3}-ZnO/Bi_2O_3/GO was assessed using *E. coli* as model bacterium under visible light. As shown in Fig 10a the percentage killing dramatically increased to 90%, on exposure of photocatalyst towards the source of visible light for 60 min. However, 10 % cell viability of *E. coli* were observed for 3 mg/ml of Eu^{+3}-ZnO/Bi_2O_3/GO under visible light Fig. 10b. The results clearly indicates the strong antibacterial activity of ternary photocatalyst against gram negative strains. Generation of ROS (e^-, h^+ $O_2^{\bullet -}$, $OH^{\bullet}$) during the photocatalytic process plays a crucial role in photocatalytic antibacterial performance [41]. Thus, to explore the role of generated ROS, scavenging experiments were performed to traps the ROS as shown in Fig. 10c. Isopropyl alcohol, ammonium oxalate, Cr(VI), and benzoquinone were used as scavengers for hydroxyl radical, holes, electron, and superoxide radical anion, respectively [42-43]. It can be clearly depicted from Fig. 10c that hydroxyl radical and superoxide radical were the chief oxidizing species responsible for antibacterial activity on 0.5mM optimized scavenging concentration [16]. Addition of isopropanol and benzoquinone traps the $OH^{\bullet}$ and $O_2^{\bullet -}$ from the reaction system, thus found very small decrease in cell viability.

4. Conclusion

In summary, Eu^{3+}-ZnO/Bi_2O_3/GO a ternary heterojunction was successfully fabricated via precipitation method. The photocatlytic efficiency of type-II heterojunction were eveluated against DMP and antibacterial property were assessed against *E. coli* under visible light source. Doping of ZnO with Eu^{3+} lowers the band gap of ZnO as compared to un-doped ZnO, further confirmed by band gap analysis. In the ternary heterojunction Bi_2O_3 and graphene oxide sheets traps electron from ZnO conduction band, thereby decreasing rate of recombination as validate by PL results. Moreover, integration of Eu^{3+}-ZnO with Bi_2O_3 extend the absorption towards visible region. With

the simultaneous adsorption and photodegradation (A+P) process, the novel ternary heterojunction was capable of degrading 98 % of DMP in 100 min. Nearly, 78% of CO_2 removal were estimated for DMP mineralization which further aid the mineralization process. The extent of mineralization also established by HPLC and LCMS analysis. Similarly, nearly 90% of *E. coli* were killed when the photocatalyst were exposed to visible light source for 60 min. The mineralization obeys pseudo-first order model. Further, scavenging experiments reveals that $OH^{\bullet}$ and $O_2^{\cdot -}$ were the principal oxidizing species responsible for mineralization. Also, the nanocomposites were recyclable up to six consecutive cycles this maintain the cost effectiveness of the photocatalyst. Thus, Eu^{3+}-ZnO/Bi_2O_3/GO nanocomposites can be easily applied for the detoxification of pollutant present in water.

References:

[1] P. Shandilya, D. Mittal, M. Soni, P. Raizada, A. Hosseini-Bandegharaei, A.K. Saini, P. Singh, Fabrication of fluorine doped graphene and $SmVO_4$ based dispersed and adsorptive photocatalyst for abatement of phenolic compounds from water and bacterial disinfection, J. Clean. Prod. 203 (2018) 386-399.

[2] P. Shandilya, D. Mittal, A. Sudhaik, M. Soni, P. Raizada, A.K. Saini, P. Singh, $GdVO_4$ modified fluorine doped graphene nanosheets as dispersed photocatalyst for mitigation of phenolic compounds in aqueous environment and bacterial disinfection, Sep. Purif. Technol. 210 (2019) 804-816.

[3] B. Pare, S.B. Jonnalagadda, H. Tomar, P. Singh, V.W. Bhagwat, ZnO assisted photocatalytic degradation of acridine orange in aqueous solution using visible irradiation, Desalin. 232 (2008) 80-90.

[4] P. Carroll, A. Myles, B. Quilty, D.E. McCormack, R. Fagan, S.J. Hinder, D.D. Dionysiou, S.C. Pillai, Antibacterial properties of F-doped ZnO visible light photocatalyst, J. Hazard. Mater. 324 (2017) 39-47.

[5] S. Gautam, P. Shandilya, V.P. Singh, P. Raizada, P. Singh, Solar photocatalytic mineralization of antibiotics using magnetically separable $NiFe_2O_4$ supported onto graphene sand composite and bentonite, J. Water Process Eng. 14 (2016) 86-100.

[6] Y. Yuan, G.F. Huang, W.Y. Hu, D.N. Xiong, B.X. Zhou, S. Chang, W.Q. Huang, Construction of g-C_3N_4/CeO_2/ZnO ternary photocatalysts with enhanced photocatalytic performance, J Phys. Chem. of Solids. 106 (2017) 1-9.

[7] J.H. Xiao, W.Q. Huang, Y.S. Hu, F. Zeng, Q.Y. Huang, B.X. Zhou, A. Pan, K. Li, G.F. Huang, Facile in situ synthesis of wurtzite ZnS/ZnO core/shell heterostructure with highly efficient visible-light photocatalytic activity and photostability, J Phys. D Appl. Phys. 51(7) (2018) 075501.

[8] P. Raizada, P. Singh, A. Kumar, G. Sharma, B. Pare, S.B. Jonnalagadda, P. Thakur, Solar photocatalytic activity of nano-ZnO supported on activated carbon or brick grain particles: role of adsorption in dye degradation, Appl. Catal. A, 486 (2014) 159-169.

[9] O. Yayapao, T. Thongtem, A. Phuruangrat, S. Thongtem, Sonochemical synthesis of Dy-doped ZnO nanostructures and their photocatalytic properties, J. Alloys Comp. 576 (2013) 72-79.

[10] A.R. Khataee, A. Karimi, R.D.C. Soltani, M. Safarpour, Y. Hanifehpour, S.W. Joo, Europium-doped ZnO as a visible light responsive nanocatalyst: Sonochemical synthesis, characterization and response surface modeling of photocatalytic process, Appl. Catal. A: Gen. 488 (2014) 160–170.

[11] P. M. Aneesh, M. K. Jayaraj, Red luminescence from hydrothermally synthesized Eu-doped ZnO nanoparticles under visible excitation, Bull. Mater. Sci.33 (2010) 227–231.

[12] A. Hernandez-Gordillo, J.C. Medina, M. Bizarro, R. Zanella, B.M. Monroy, S.E. Rodil, Photocatalytic activity of enlarged microrods of alpha-Bi2O3 produced using ethylenediamine-solvent, Ceram Int. 42(10) (2016) 11866–75.

[13] B. Priya, P. Raizada, N. Singh, P. Thakur, P. Singh, Adsorptional photocatalytic mineralization of oxytetracycline and ampicillin antibiotics using Bi_2O_3/BiOCl supported on graphene sand composite and chitosan, J. Colloid Interface Sci. 479 (2016) 271-283.

[14] S. Balachandran, M. Swaminathan, Facile fabrication of heterostructured Bi_2O_3–ZnO photocatalyst and its enhanced photocatalytic activity, J. Phys. Chem. C, 116 (50) (2012) 26306-12.

[15] Y. Yang, L. Xu, C. Su, J. Che, W. Sun, H. Gao, ElectrospunZnO/Bi_2O_3 nanofibers with enhanced photocatalytic activity, J Nanomater. 2014 (2014) 7.

[16] P. Shandilya, D. Mittal, M. Soni, P. Raizada, J.H. Lim, D.Y. Jeong, D.P. Dewedi, A.K. Saini, P. Singh, Islanding of $EuVO_4$ on high-dispersed fluorine doped few layered graphene sheets for efficient photocatalytic mineralization of phenolic compounds and bacterial disinfection, J. Taiwan Inst. Chem. Eng. (2018) 1-15.

[17] A. Khataee, A. Karimi , M. Zarei, S.W. Joo, Eu-doped ZnO nanoparticles: Sonochemical synthesis, characterization, and sonocatalytic application Ultrason. Sonochem. 2015.

[18] P. Raizada, J. Kumari, R. Dhiman, V. P. Singh, P. Singh, Magnetically retrievable Bi_2WO_6/Fe_3O_4 immobilized on graphene sand composite for investigation of photocatalytic mineralization of oxytetracycline and ampicillin, Proc. Safety Environ. Prot. 106 (2016) 104-116.

[19] APHA, Standard methods for examination of water and wastewater, American Public Health Association, American Water Works Association, Water Environment Federation New York, 6th Edn (1985) 535.

[20] M. Kolb, M. Bahadir, B. Teichgräber, Determination of chemical oxygen demand (COD) using an alternative wet chemical method free of mercury and dichromate, Water Res. 122 (2017) 645-654.

[21] S. Yi, X. Yue, D. Xu, Z. Liu, F. Zhao, D. Wang, Y. Lin, Study on photogenerated charge transfer properties and enhanced visible-light photocatalytic activity of p-type Bi_2O_3/n-type ZnO heterojunctions, New J. Chem. 39 (2015) 2917-2924.

[22] B. Priya, P. Shandilya, P. Raizada, P. Thakur, N. Singh, P. Singh, Photocatalytic mineralization and degradation kinetics of ampicillin and oxytetracycline antibiotics using graphene sand composite and chitosan supported BiOCl, J. Mol. Catal. A: Chem. 423 (2016) 400-413.

[23] R. Zhou, Q. Zhao, K.K. Liu, Y.J. Lu, L. Dong, C.X. Shan, Europium-decorated ZnO quantum dots as a fluorescent sensor for the detection of ananthrax biomarker, J. Mater. Chem. C, 5 (2017) 1685.

[24] T.V.L Thejaswini, D. Prabhakaran, M.A. Maheswari, Ultrasound assisted synthesis of nano-rod embedded petal designed a-Bi_2O_3-ZnO nanoparticles and their ultra-responsive visible light induced photocatalytic properties, J. Photochem. Photobiol. A: Chem. 335 (2017) 217-229.

[25] P. Singh, S. Gautam, P. Shandilya, B. Priya, V.P. Singh, P. Raizada, Graphene bentonite supported $ZnFe_2O_4$ as super-paramagnetic photocatalyst for antibiotic degradation. Adv. Mater. Lett. 8(3) (2017) 229-238.

[26] S. Perumbilavil, P. Sankar, T.R. Priya, R. Philip, White light Z-scan measurements of ultrafast optical nonlinearity in reduced graphene oxide nanosheets in the 400–700 nm region. Appl. Phys. Lett. 107(5) (2015) 051104.

[27] S. Kumar, R. Prakash, and Vivek K. Singh, Synthesis, characterization, and applications of europium oxide: a review, Rev. Adv. Sci. Eng. 4 (2015) 247-257.

[28] S. Kumar, A. Dhiman, P. Sudhagar, V. Krishnan, ZnO-graphene quantum dots heterojunctions for natural sunlight-driven photocatalytic environmental remediation, Appl. Surf. Sci. 447 (2018) 802-815.

[29] Y. Feng, L. Li, J. Li, J. Wang, L. Liu, Synthesis of mesoporous BiOBr 3D microspheres and their photodecomposition for toluene, J. Hazard. Mater. 192, (2011) 538-544.

[30] H. Y. Ji, X. C. Jing, Y. G. Xu, J. Yan, H. P. Li, Y. P. Li, Y. Huang, Q Zhang, H. Xu and H. M. Li, Magnetic g-C_3N_4/$NiFe_2O_4$ hybrids with enhanced photocatalytic activity, RSC Adv. 5 (2015) 57960-57967.

[31] X.J. Wang, W.Y. Yan, F.T. Li, Y.B. Xue, R.H. Liu and Y.J. Hao, In situ microwave-assisted synthesis of porous N-TiO_2/g-C_3N_4 heterojunctions with enhanced visible-light photocatalytic properties, Ind. Eng. Chem. Res., 52 (2013) 17140–17150.

[32] P. Raizada, J. Kumari, P. Shandilya, P. Singh, Kinetics of photocatalytic mineralization of oxytetracycline and ampicillin using activated carbon supported ZnO/$ZnWO_4$ nanocomposite in simulated waste water, Desalin. Water Treat. 79 (79) (2017) 204-213.

[33] P. Raizada, B. Priya, P. Thakur, P. Singh, Solar light induced photodegradation of oxytetracyline using Zr doped TiO_2/CaO based nanocomposite, Ind. J. Chem. Sec. A, 55(7) (2016) 803-809.

[34] J. He, Y. Cheng, T. Wang, D. Feng, L. Zheng, D. Shao, W. Wang, W. Wang , F. Lu , H. Dong , R. Zheng , H. Liu, Enhanced photocatalytic performances and magnetic recovery capacity of visible-light-driven Z-scheme $ZnFe_2O_4$/AgBr/Ag photocatalyst, Appl. Surf. Sci. 440 (2018) 99-106.

[35] G. Gupta, A. Kaur, A.S.K. Sinha, S.K. Kansal, Photocatalytic degradation of levofloxacin in aqueous phase using Ag/AgBr/BiOBr microplates under visible light, Mater. Res. Bull. 88 (2017) 148–155.

[36] C.B. Ong, L.Y. Ng, A.W. Mohammad, A review of ZnO nanoparticles as solar photocatalysts: Synthesis, mechanisms and applications, Renewable and Sustainable Energy Reviews 81 (2018) 536-551.

[37] M. Han, T. Sun, P.Y. Tan, X. Chen, O.K.Tan, M.S. Tse, m-$BiVO_4$@γ-Bi_2O_3 core–shell p–n heterogeneous nanostructure for enhanced visible-light photocatalytic performance, RSC Adv.3 (2013) 24964-24970.

[38] J.C. Medina, N.S. Portillo-Velez, M. Bizarro, A. Hernández-Gordillo, S.E. Rodil, Synergistic effect of supported ZnO/Bi_2O_3 heterojunctions for photocatalysis under visible light, Dyes and Pigments 153 (2018) 106–116.

[39] A. Mehdinia, M. Ahmadifar, M.O. Aziz-Zanjani, A. Jabbari, M.S. Hashtroudi, Selective adsorption of 2, 4-dinitrophenol on molecularly imprinted nanocomposites of mesoporous silica SBA-15/polyaniline. Analyst, 137(18) (2012) 4368-4374.

[40] L.S. Andrade, E.A. Laurindo, R.V.D. Oliveira, R.C. Rocha-Filho, Q.B. Cass, Development of a HPLC method to follow the degradation of phenol by electrochemical or photo-electrochemical treatment. J. Braz. Chem. Soc., 17(2) (2006) 369-373.

[41] P. Raizada, A. Sudhaik, P. Shandilya, A. Saini, V. Gupta, P. Singh, Fabrication of Ag_3VO_4 decorated phosphorus and sulphur co-doped graphitic carbon nitride as high-dispersed photocatalyst for phenol mineralization and *E.Coli* disinfection, Sep. Purify.Technol. 212 (2018) 887-900.

[42] P. Raizada, A. Sudhaik, P. Singh, P. Shandilya, P. Thakur, H. Jung. Visible light assisted photodegradation of 2, 4-dinitrophenol using Ag_2CO_3 loaded phosphorus and sulphur co-doped graphitic carbon nitride nanosheets in simulated wastewater. Arab. J. Chem. (2018).

[43] P. Singh, P. Raizada, A. Suadhik, P. Shandilya, P. Thakur, S. Agarwal, V.K. Gupta, Enhanced photocatalytic activity and stability of AgBr/BiOBr/graphene heterojunction for phenol degradation under visible light, J Saudi Chem. Soc. 23 (2018) 586-599.

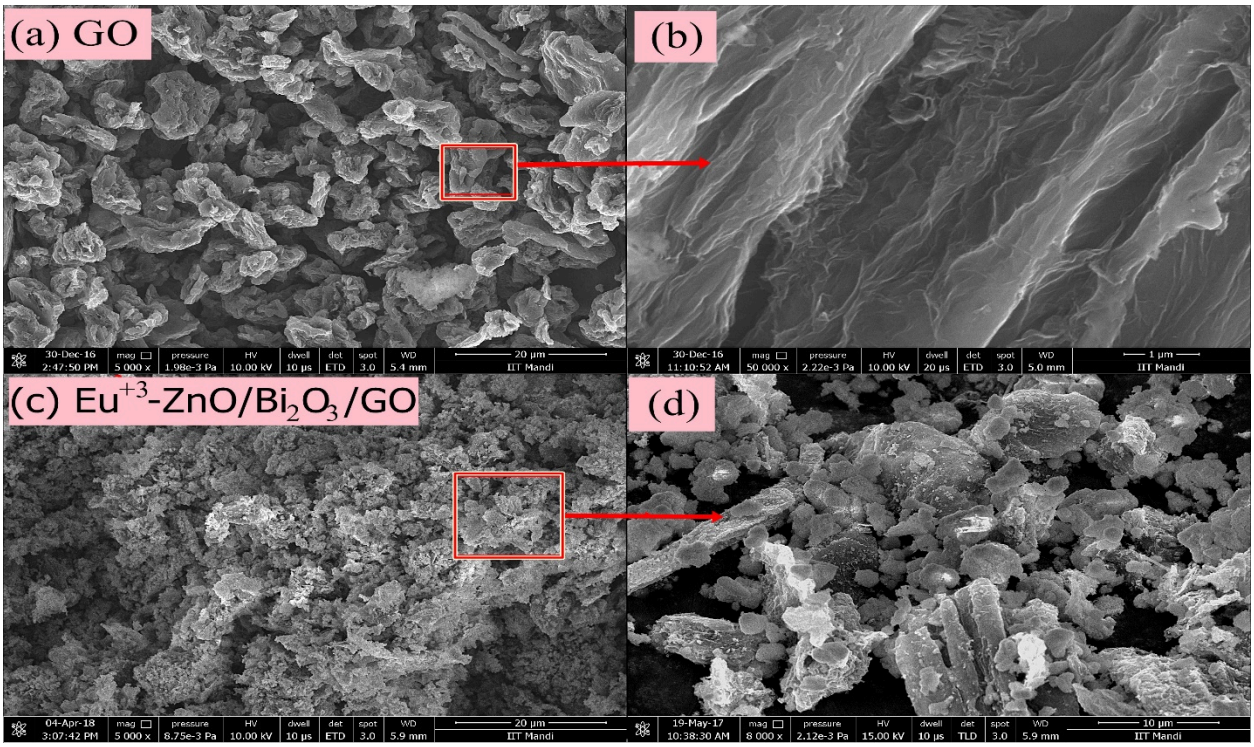

Fig. 1. FESEM images of (a) GO (b) magnified image of slected portion of (a), (c) Eu^{3+}-$ZnO/Bi_2O_3/GO$ and (d) magnified image of slected portion of (c).

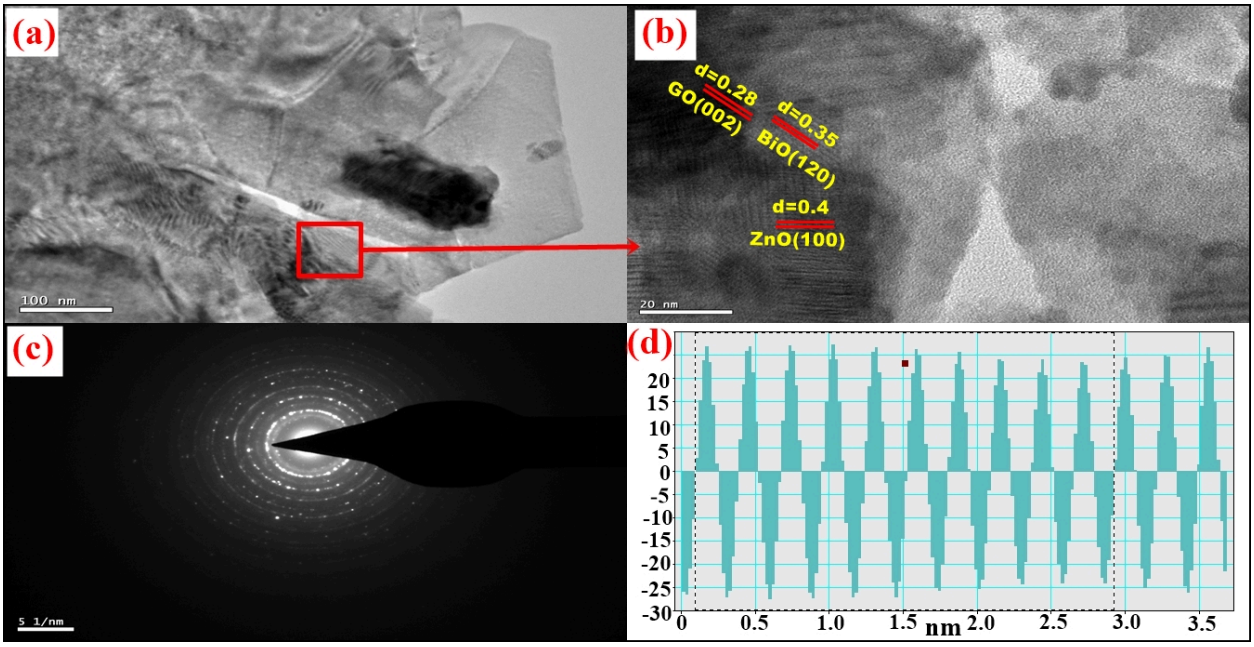

Fig. 2.(a) TEM images of Eu^{3+}-$ZnO/Bi_2O_3/GO$ (b) magnified image of slected portion of (a), (c) SAED pattern of Eu^{3+}-$ZnO/Bi_2O_3/GO$ and (d) planar spacing of the composite.

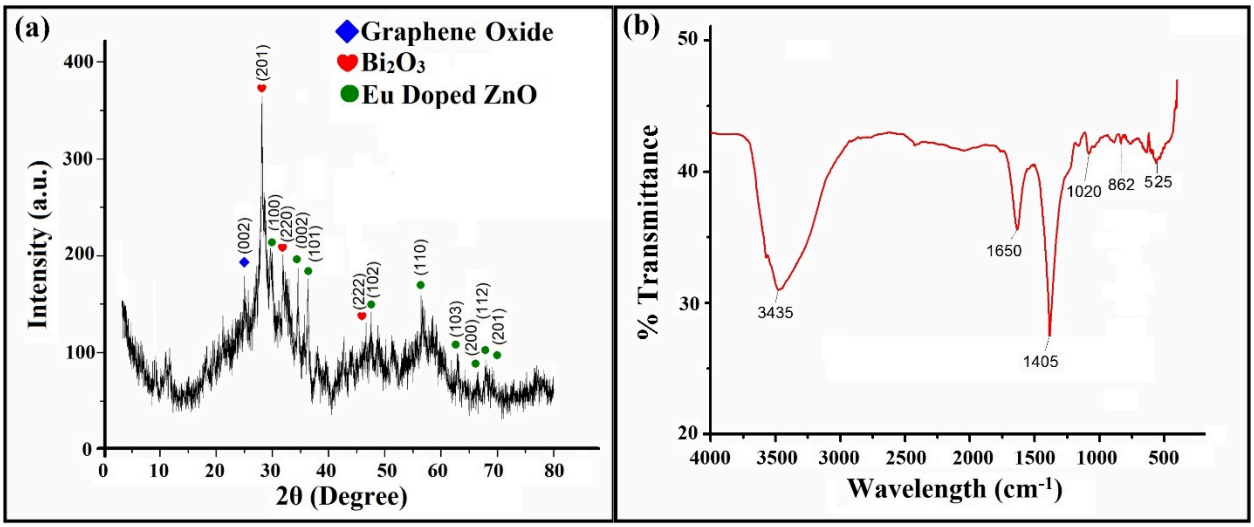

Fig. 3. XRD and FTIR spectra of Eu^{3+}-ZnO/Bi_2O_3/GO nanocomposite.

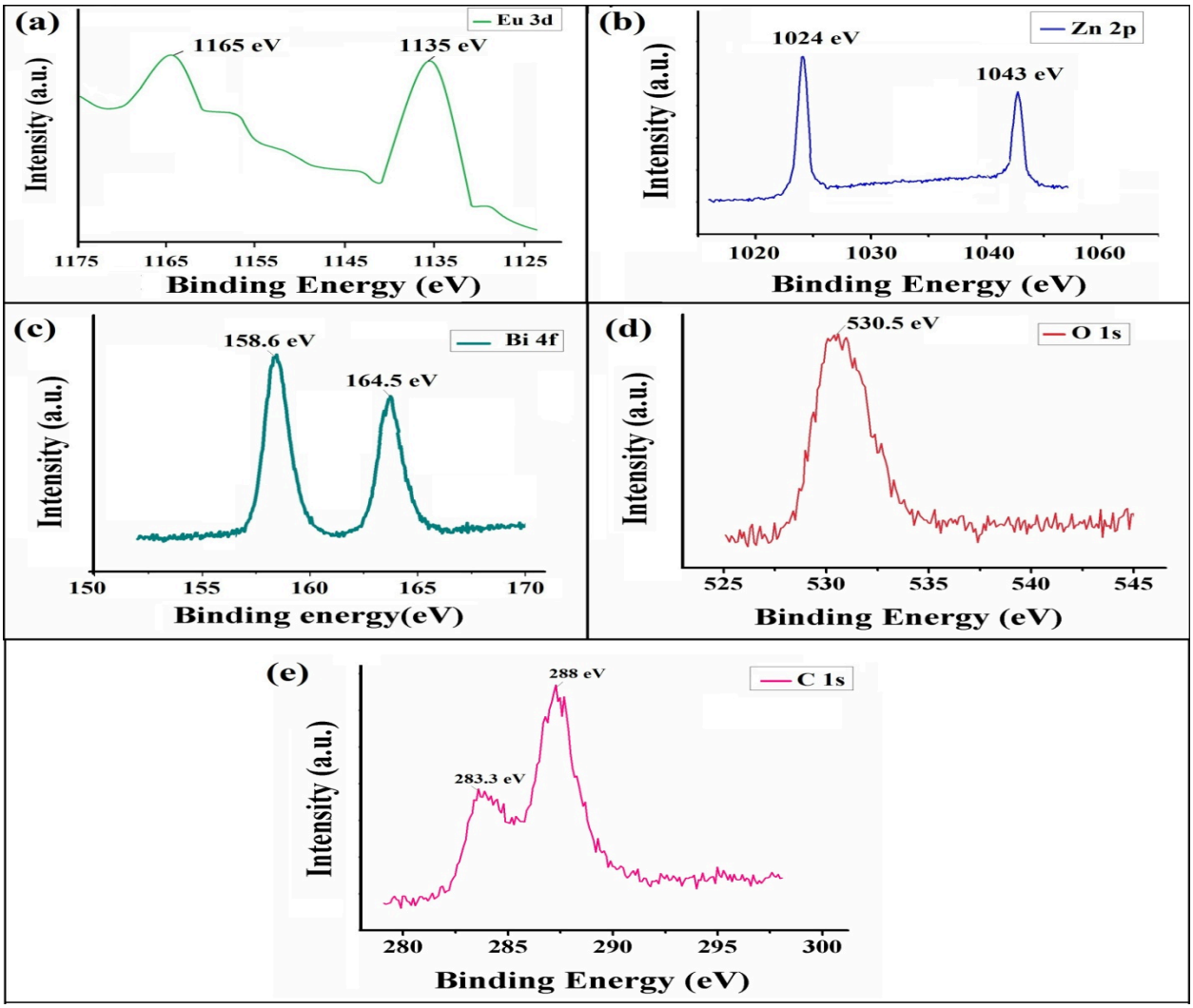

Fig. 4. XPS spectra of Eu^{3+}-ZnO/Bi_2O_3/GO nanocomposite.

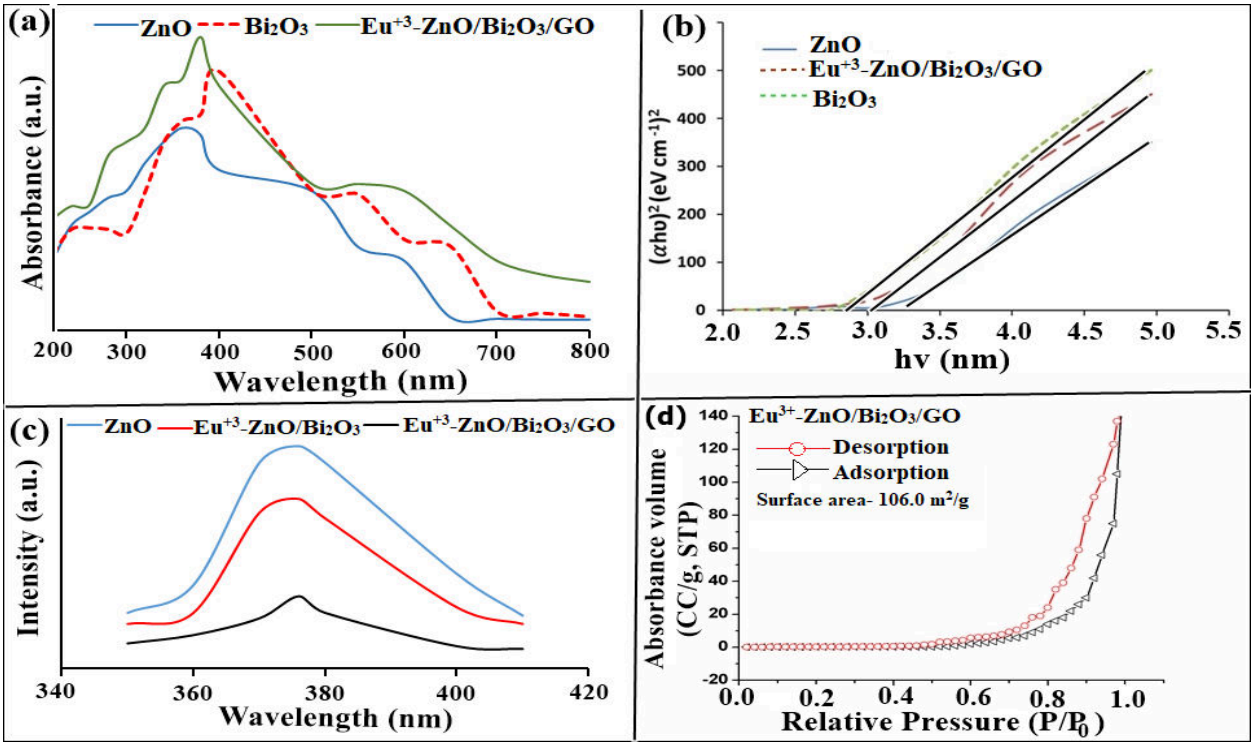

Fig. 5. (a) UV-visible analysis, (b) Band gap calcluation, (c) photoluminescence anlysis and (d) BET adsorption-desorption isotherms of Eu^{3+}-ZnO/Bi_2O_3/GO.

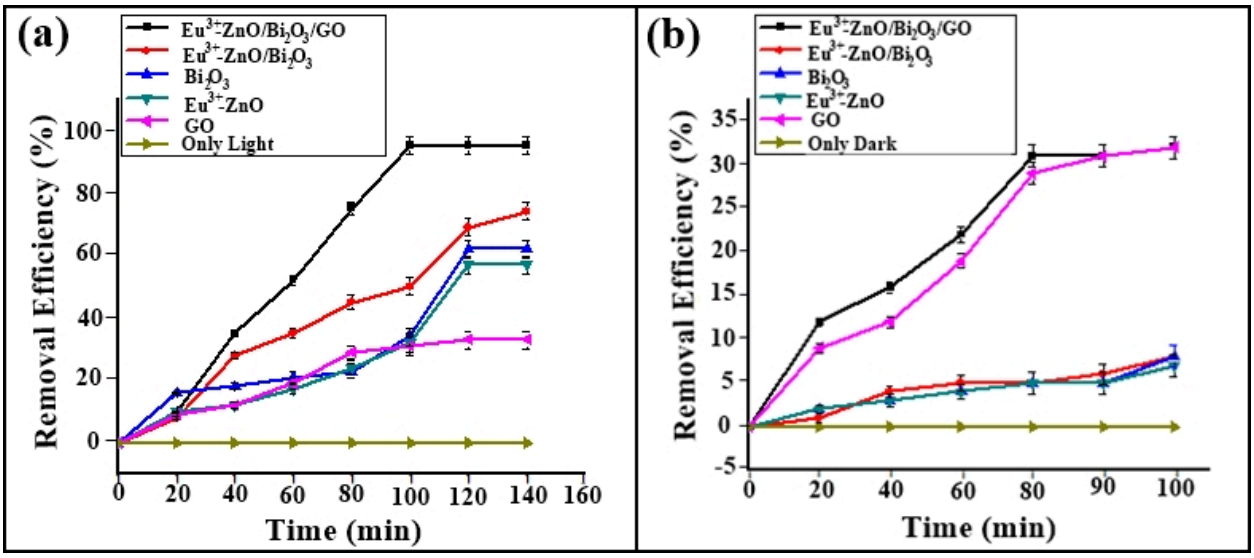

Fig. 6. (a) Photocatalytic degrdation of DMP and (b) adsoprtional removal of DMP using Eu^{3+}-ZnO/Bi_2O_3/GO [Reaction conditions: initial reaction pH= 4.0; [DMP] = 1×10^{-3} mol dm^{-3}; [photocatalyst] = 50 mg/100 mL; and intensity of light = 750 lx].

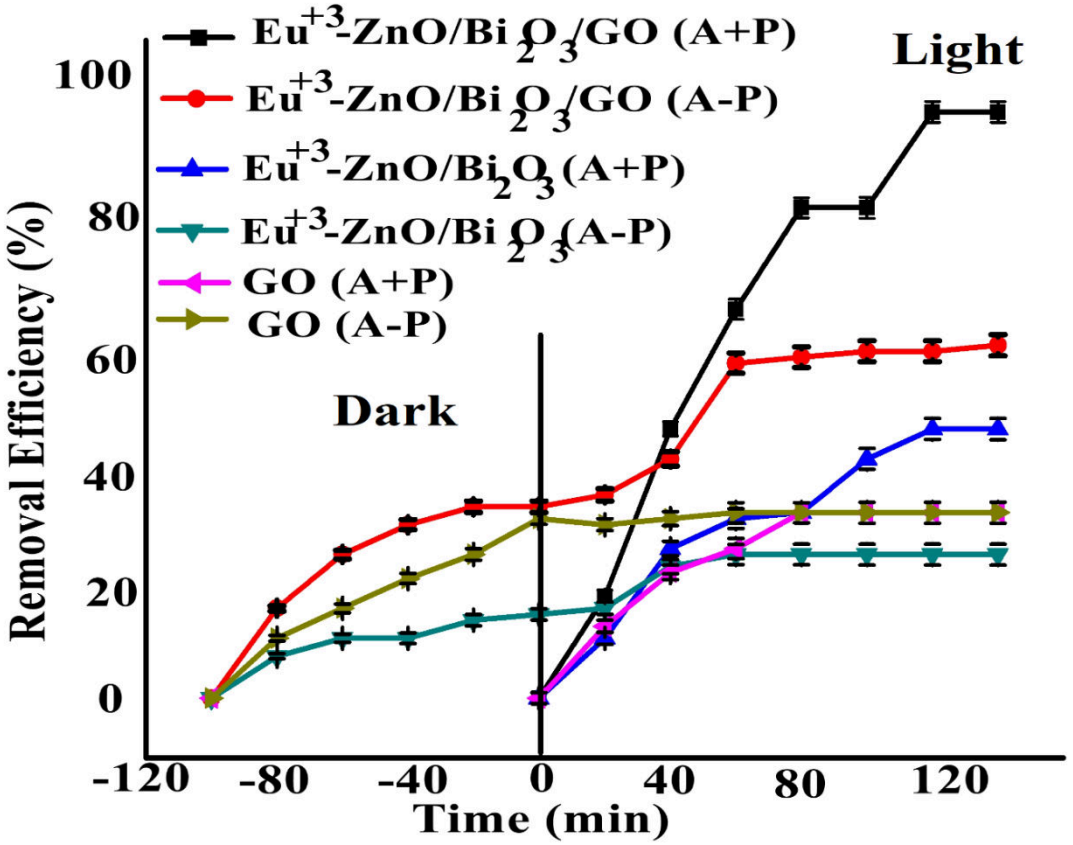

Fig. 7. Effect of adosprtion on photodegrdation of DMP using Eu^{3+}-ZnO/Bi_2O_3/GO. [Reaction conditions: initial reaction pH= 4.0; [DMP] = 1×10^{-3} mol dm^{-3}; [photocatalyst] = 50 mg/100 mL; and intensity of light = 750 lx].

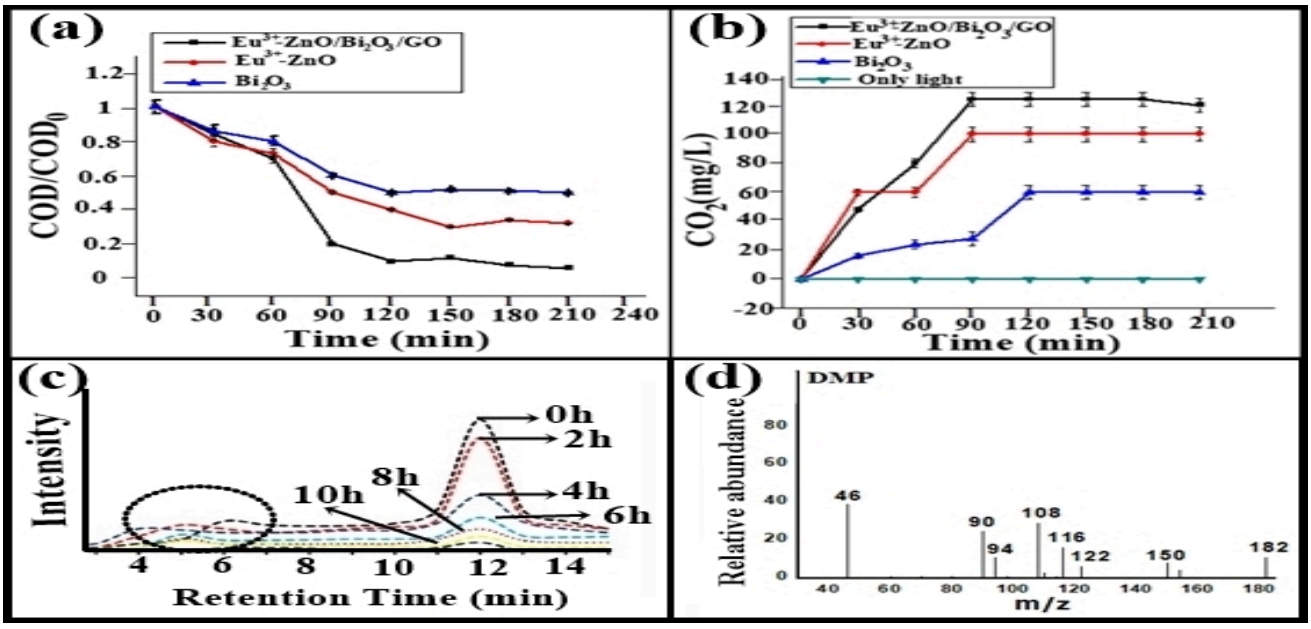

Fig. 8. (a) COD removal (b) CO_2 estimation, (c) HPLC and (d) LCMS analysis of Eu^{3+} ZnO/Bi_2O_3/GO [Reaction conditions: initial reaction pH= 4.0; [DMP] = 1×10^{-3} mol dm^{-3}; [photocatalyst] = 50 mg/100 mL; and intensity of light = 750 lx].

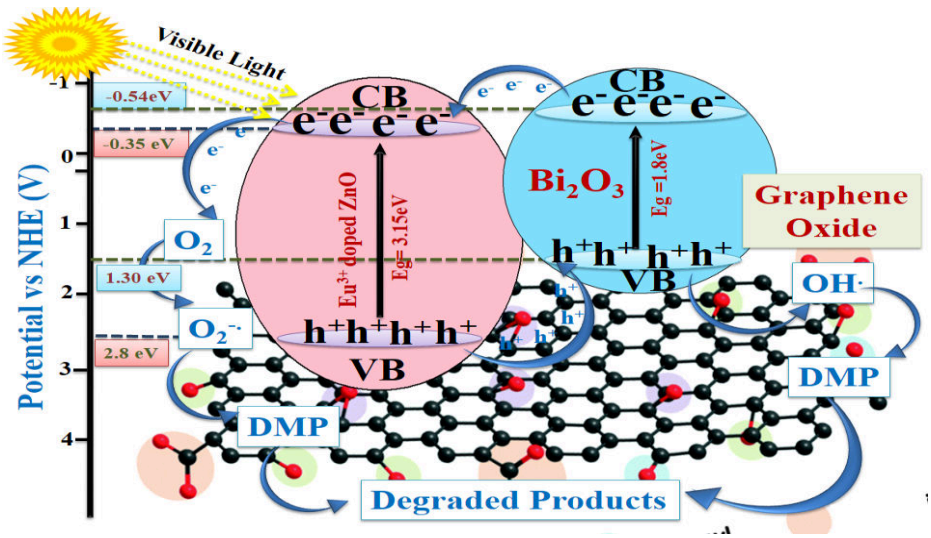

Fig. 9. Mechanistic view for enmanced photocatalytic degradation of DMP

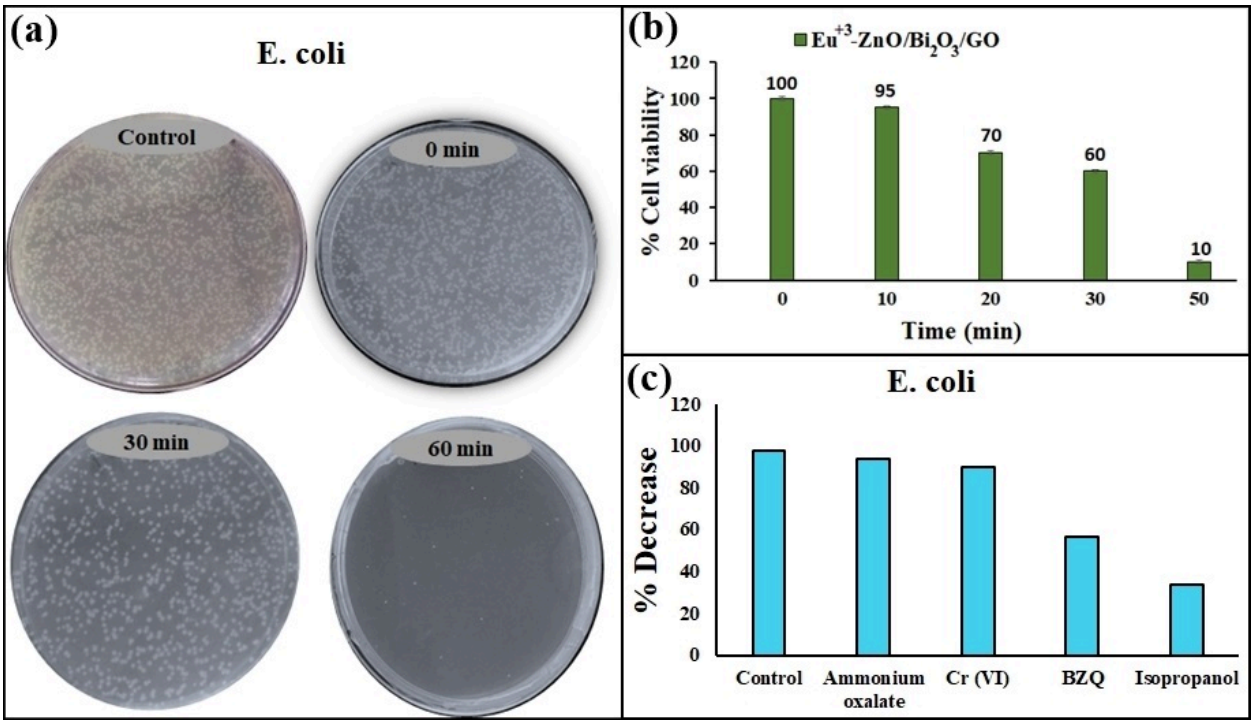

Fig. 10. (a) Antibacterial study of Eu^{+3}-ZnO/Bi_2O_3/GO against *E. coli* by CFU method in the presence of visible light, (b) percentage cell viability under different time of light exposure of

Eu^{+3}-ZnO/Bi_2O_3/GO, (c) Effect of radical scavengers on photocatalytic antibacterial activity of Eu^{+3}-ZnO/Bi_2O_3/GO. [Reaction time = 1 h; light intensity = 750 lx; (c) Scavenger concentration: 0.5mM of isopropanol, benzoquinone, ammonium oxalate, Cr(VI) for 0.5 mg/ml of Eu^{+3}-ZnO/Bi_2O_3/GO under solar light irradiation].

Supplementary Figures (SSSCIE_2020_148R2)

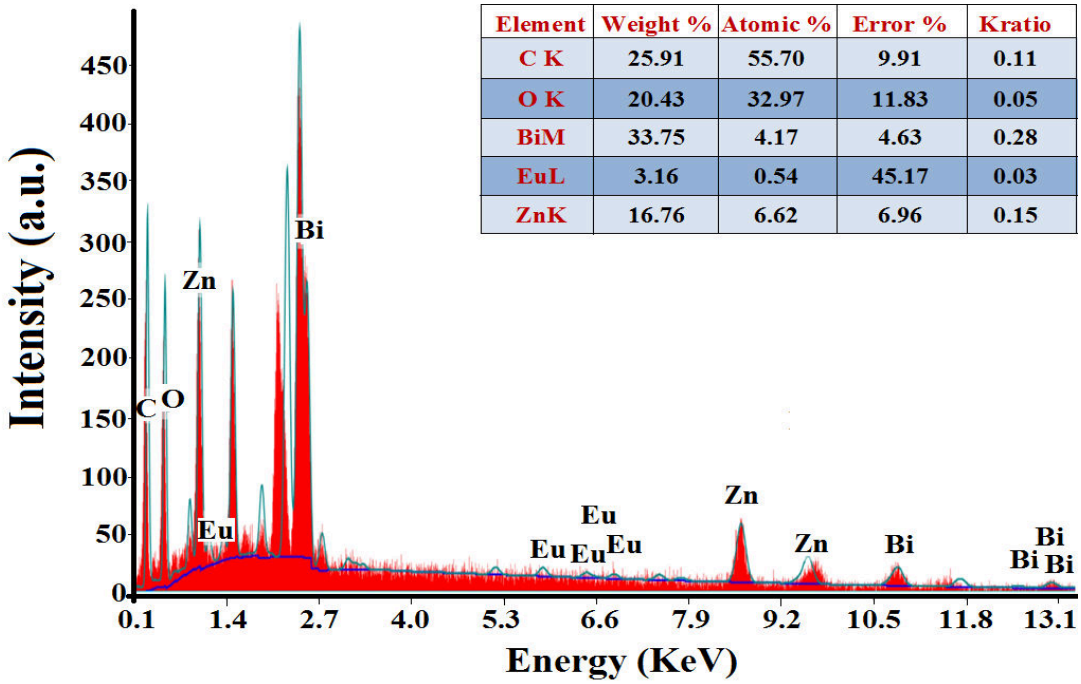

Fig. S1. EDX spectrum o f Eu^{3+}-ZnO/Bi_2O_3/GO nanocomposite.

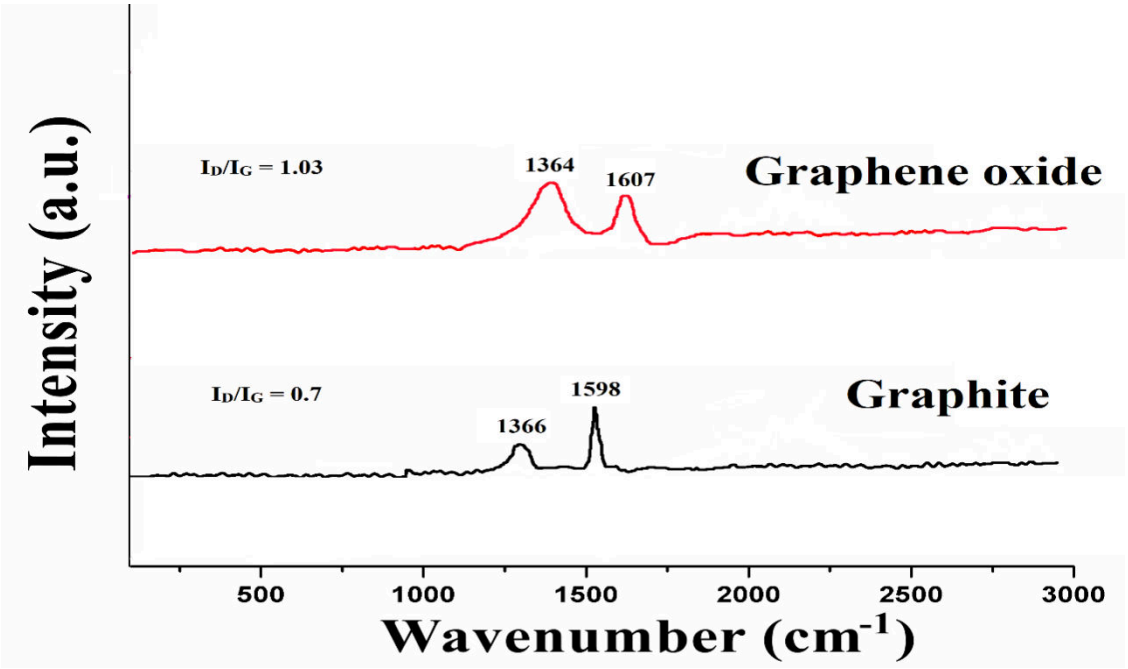

Fig. S2. Raman analysis of Graphite and graphene oxide.

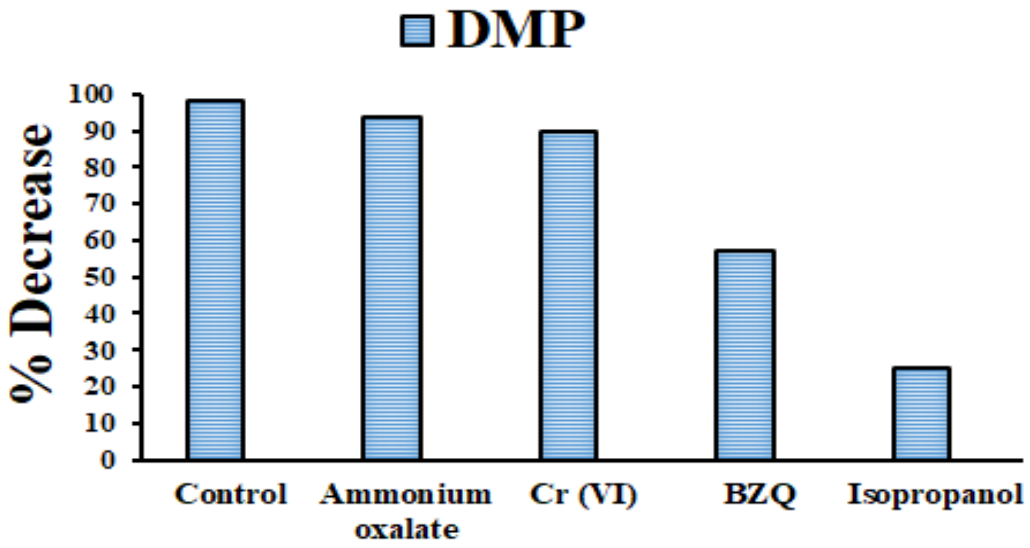

Fig. S3. Effect of radical scavengers on DMP degradation by using Eu^{3+}-ZnO/Bi_2O_3/GO.

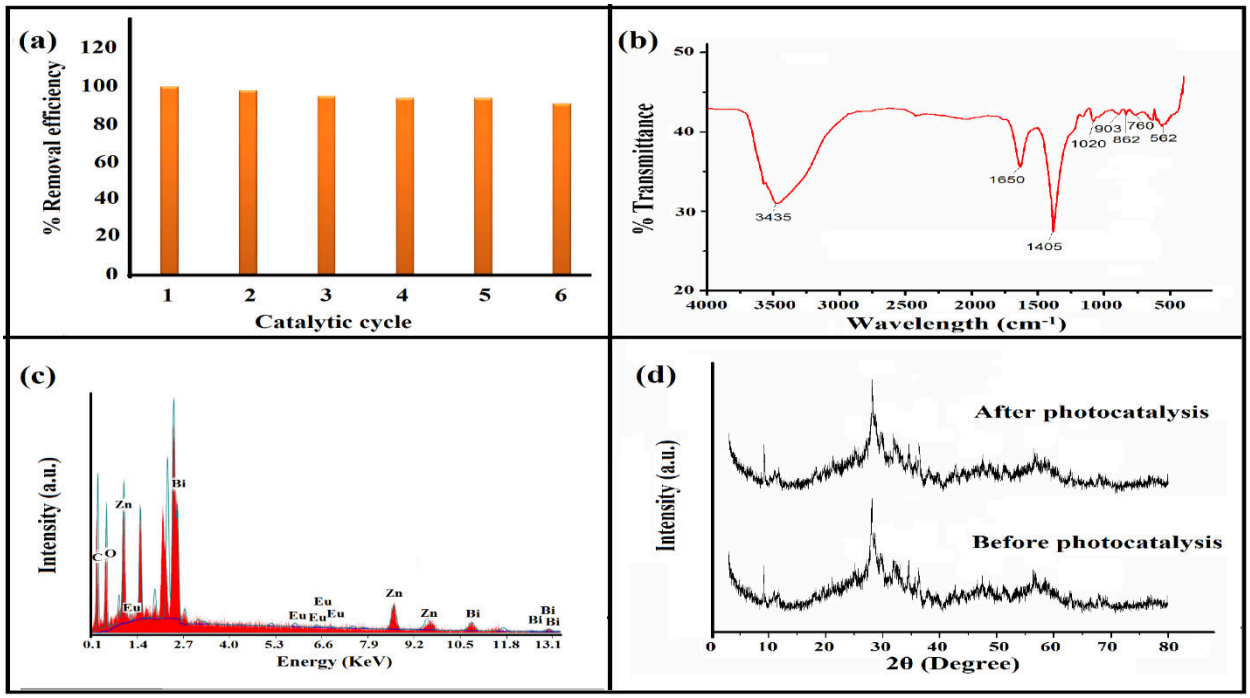

Fig. S4. (a) Recycle efficieny of Eu^{3+}-ZnO/Bi_2O_3/GO (b) FTIR spectra of Eu^{3+}-ZnO/Bi_2O_3/GO after photocatalysis (c) EDX analysis of Eu^{3+}-ZnO/Bi_2O_3/GO after photocatalysis and (d) XRD pattern of Eu^{3+}-ZnO/Bi_2O_3/GO before and after photocatalysis [Reaction conditions: initial reaction pH= 4.0; [DMP] = 1×10^{-3} mol dm^{-3}; [photocatalyst] = 50 mg/100 mL; and intensity of light = 750 lx].